Imaging the subcellular viscoelastic properties of mouse oocytes

Guillaume Flé[a], Elijah Van Houten[b] (iD), Gaudeline Rémillard-Labrosse[c], Greg FitzHarris[c,d], and Guy Cloutier[a,e,1] (iD)

In recent years, cellular biomechanical properties have been investigated as an alternative to morphological assessments for oocyte selection in reproductive science. Despite the high relevance of cell viscoelasticity characterization, the reconstruction of spatially distributed viscoelastic parameter images in such materials remains a major challenge. Here, a framework for mapping viscoelasticity at the subcellular scale is proposed and applied to live mouse oocytes. The strategy relies on the principles of optical microelastography for imaging in combination with the overlapping subzone nonlinear inversion technique for complex-valued shear modulus reconstruction. The three-dimensional nature of the viscoelasticity equations was accommodated by applying an oocyte geometry-based 3D mechanical motion model to the measured wave field. Five domains—nucleolus, nucleus, cytoplasm, perivitelline space, and zona pellucida—could be visually differentiated in both oocyte storage and loss modulus maps, and statistically significant differences were observed between most of these domains in either property reconstruction. The method proposed herein presents excellent potential for biomechanical-based monitoring of oocyte health and complex transformations across lifespan. It also shows appreciable latitude for generalization to cells of arbitrary shape using conventional microscopy equipment.

oocyte viscoelasticity imaging | oocyte biomechanics | elastic waves | microelastography | optical image reconstruction

Stiffness and viscosity changes in biological tissues have long been associated with various biomechanisms and diseases at the macroscales (1–3) and microscales (4–10). In recent years, substantial efforts have been deployed in the field of reproductive science to identify efficient mechanical biomarkers of oocytes' and embryo's developmental potential (7, 11–13). Notably, Yanez et al. (7) used a bulk assessment technique to demonstrate that a viscoelastic mechanical characterization differentiated viable versus nonviable embryos and predicted blastocyst formation within hours of fertilization, which visual examination of the zygotes failed to achieve. A multiparameter viscoelastic characterization, as opposed to purely elastic, was found necessary to achieve this differentiation and was observed to provide a greater discriminating power than the individual elastic properties on their own. Mechanical changes in oocytes were also measured during maturation and correlated with the embryo's development. In particular, the zona pellucida (ZP) was found to soften during maturation and stiffen after fertilization, which is likely to influence the oocyte's permeability to sperm (7, 14–16). Cortex-tension-driven spindle migration and positioning during the asymmetric division of oocyte meiosis (17, 18) is another example supporting the relevance of oocyte stiffness monitoring, as overly soft oocytes were observed to correlate with chromosome misalignment, which is predictive of aneuploidy (19, 20). Viscosity, notably more difficult to characterize than simple elastic stiffness, has mostly been assessed in the cytoplasm. Main findings underline changes in cytoplasm viscosity from aqueous to viscous during maturation (concomitant with ZP softening) (21), the viscosity dependence of oocyte spherical shape restoration after intracytoplasmic sperm injection (ICSI), and a hindered development in oocytes with increased cytoplasmic viscosity (22). Overall, both stiffness and viscosity demonstrate potential as quantifiable measures of oocyte quality. The establishment of a correlation between cell biomechanics and cellular health raises the need for adapted mechanical characterization tools (12).

Current oocyte stiffness micromeasurement technologies essentially capitalize on the deformability of a material under tightly controlled external loads. In micropipette aspiration (7), compression (23), and indentation (16, 24–27) techniques, a pipette is brought in contact with the oocyte, and the induced geometrical deformation is analyzed and fitted to a rheological model. The levels of stress applied to the oocyte are often high, and the sensitivity to mechanical contrast is limited due to the global stiffness assessment approach (notable exception: ref. 23). Similar indentation versus deformation principles

Significance

In reproductive science, viable and nonviable oocytes may be distinguished by the characterization of their concomitant elastic and viscous properties. However, the bulk characterization and high levels of cell deformation required with standard techniques hinder the nondestructive identification of cell structures and their contribution to developmental success. Using ultrafast microelastography and an optimization-based reconstruction technique, maps of oocyte viscoelasticity were produced noninvasively. The continuum model allowed for a complete viscoelastic description of the medium, free of rheological assumptions and restrictive approximations on the measured data. This robust approach may ultimately be of use to help establish viscoelasticity-based guidelines for egg selection in medically assisted reproduction procedures.

apply to atomic force microscopy (AFM) (28, 29), which uses lower deformation rates and allows assessing cell surface boundaries with submicron resolutions (30). Overall, both technologies often require cell dissection to isolate regions of interest (17, 28) and involve slow experimental procedures, potentially hindering the detection of faster biomechanical processes. To our knowledge, oocyte viscosity has only been measured globally through pipette indentation (7) or invasively in the vicinity of cytoplasmic endogenous vesicles using optical tweezers (31) and through the analysis of the size and persistence of an injection funnel after ICSI (22), wherein larger and more persistent funnels are indicative of greater cytoplasmic viscosity.

Approaches to probe the biomechanics of different cell types, including particle tracking microrheology, cell indentation (local or global), optical trap, and bead-based techniques, have been reviewed and compared in ref. 32. In these examples, estimated elastic and viscous parameters showed a wide disparity (100 to 1,000-fold variations, respectively) due to the different experimental procedures involved. Alternatively, microfluidic-based (33–36) and optical (37–39) techniques have been introduced. Notably, optical microelastography (OME) relies on the analysis of induced high-frequency elastic wave patterns using standard bright-field microscopy imaging and a high-speed camera (39). However, the pure shear wave assumption invoked in previous work is strongly challenged in the context of tiny confined cellular domains, which invalidates the conversion of wave parameters (wavelength λ or speed c) into a material mechanical property (shear stiffness μ_s) through the elastic relationship $\mu_s = \rho c^2$, where ρ is the material's density (40). Additionally, the reconstruction of wave parameters through time-reversal-based techniques is also challenged in highly attenuating cellular media where the time symmetry of the undamped wave propagation equation is no longer fulfilled.

Here, we detail a robust strategy to image the viscoelastic properties of oocytes, noninvasively and at a subcellular level, through the reconstruction of the fully distributed storage and loss moduli. The method is applied to live mouse oocytes and numerical simulations and is based on OME and the overlapping subzone nonlinear inversion (NLI) technique, an optimization scheme for mechanical parameter identification. The generalized mechanical model involved allows for a heterogeneous viscoelastic description of the material, as opposed to wave characterization, and circumvents shear wave and rheology-based assumptions while eliminating the noise-enhancing operations performed in standard direct inversion techniques. To our knowledge, multiparametric viscoelasticity mapping at the subcellular scale has not been reported previously and represents a significant advance in microelastography. Fig. 1*A* shows the OME experimental setup. On the platform of an inverted microscope mounted with a 100× lens, the oocyte was lightly contracted by two retention micropipettes connected to micromanipulators for positioning. The pipette on the left-hand side resembled a standard ICSI "holding pipette" and was used to immobilize the oocyte, while the right-hand side was laterally pulsed by a piezo-electric crystal providing a 14.4-kHz harmonic in-plane actuation. The pulsing pipette induced mechanical elastic waves visualized as local structural deformations traveling across the cell. The deformations were captured in the focal plane, set to cut through the center of the oocyte, by a high-speed camera and converted into local in-plane displacement values quantifying the deviations of the pulsed geometry from the shape of the oocyte at rest. Then, a full-field displacement dataset, i.e., three motion components (u, v, and w) in three contiguous planes,

was approximated from the measured in-plane data using a 3D oocyte geometry-based displacement model. The model relied on the symmetrical nature of germinal vesicle-stage (GV) oocytes, the near-incompressibility property of biological tissues, and the in-plane actuation in the imaged slice. Fig. 1*B* shows a schematic view of the harmonic actuation displacement estimation. See the Methods section for more details. Displacement data were then processed with the finite element-based overlapping subzone nonlinear inversion technique (41, 42). Here, oocytes were modeled as a heterogeneous, viscoelastic, nearly incompressible, isotropic material. The optimization-based inversion procedure and the boundary value problem relating the material's mechanical parameters to the measured displacement field are detailed in the Methods section. Advantages of NLI over other reconstruction techniques are discussed and illustrated in *SI Appendix*, Note 1 and Fig. S1.

Results

The preprocessing step for full-field displacement approximation and the inversion procedure were first applied to synthetic data. This numerical study allowed us to test the overall pipeline and analyze the performance of the iterative inversion with the experiment-based actuation frequency $f = 14.4$ kHz and with mechanical property distributions of relative magnitudes. Two scaled distributions were used, $\mu_1 = 2.5 \times \mu_{\exp}$ and $\mu_2 = \mu_{\exp}$, where $\mu_{\exp}$ refers to the mechanical properties observed in experiments (*Methods* for details). Fig. 2 shows storage (μ_r) and loss (μ_i) modulus reconstructions performed on displacements provided by a finite element simulation of an oocyte domain made of four concentric spherical structures (nucleolus, nucleus, cytoplasm, and ZP). As in experiments, in-plane motion data were processed with the 3D displacement model. The 30-μm zone size used in NLI and the wavelength of the elastic field are illustrated in the first column of both Fig. 2*A* and *B*. The second columns indicate the true mechanical properties used in the simulations, and the third columns show reconstructions using simulation-based approximated full-field displacements. The basis for full-field displacement approximation is presented in *SI Appendix*, Note 2 and Fig. S2. Computational steps are detailed in *Methods*.

Then, 21 freshly collected live oocytes underwent the microelastography pipeline. Fig. 3*A* shows anatomical and segmentation images of a representative oocyte. On the 21 oocyte datasets treated, all storage modulus and 13 loss modulus identifications converged to stable distributions ($\mu_{r,fc}$ and $\mu_{i,fc}$, respectively, where *fc* stands for fully converged), and 8 loss modulus reconstructions continued to progress toward lower values ($\mu_{i,pc}$, where *pc* stands for partially converged). Fig. 3 *B*, *C*, and *D* show the average values in main oocyte regions nucleolus, nucleus, cytoplasm, perivitelline space (PS), and ZP for each convergence profile (fully and partially converged). Fig. 3 *E* and *F* show anatomical and segmentation images of two representative oocytes along with complex-valued shear modulus reconstructions where full- and partial-convergence were observed, respectively. *SI Appendix*, Note 3 and Fig. S3 present the convergence profiles of these reconstructions.

Table 1 reports *P*-values obtained using a Wilcoxon rank sum test to quantify the statistical difference between each region for the fully and partially converged reconstructions. A Bonferroni correction was applied to a significance base level $\alpha_0 = 0.05$ to account for the ten reported comparisons. The corrected significance level was $\alpha_{corr.} = 0.05/10 = 0.005$. Significant
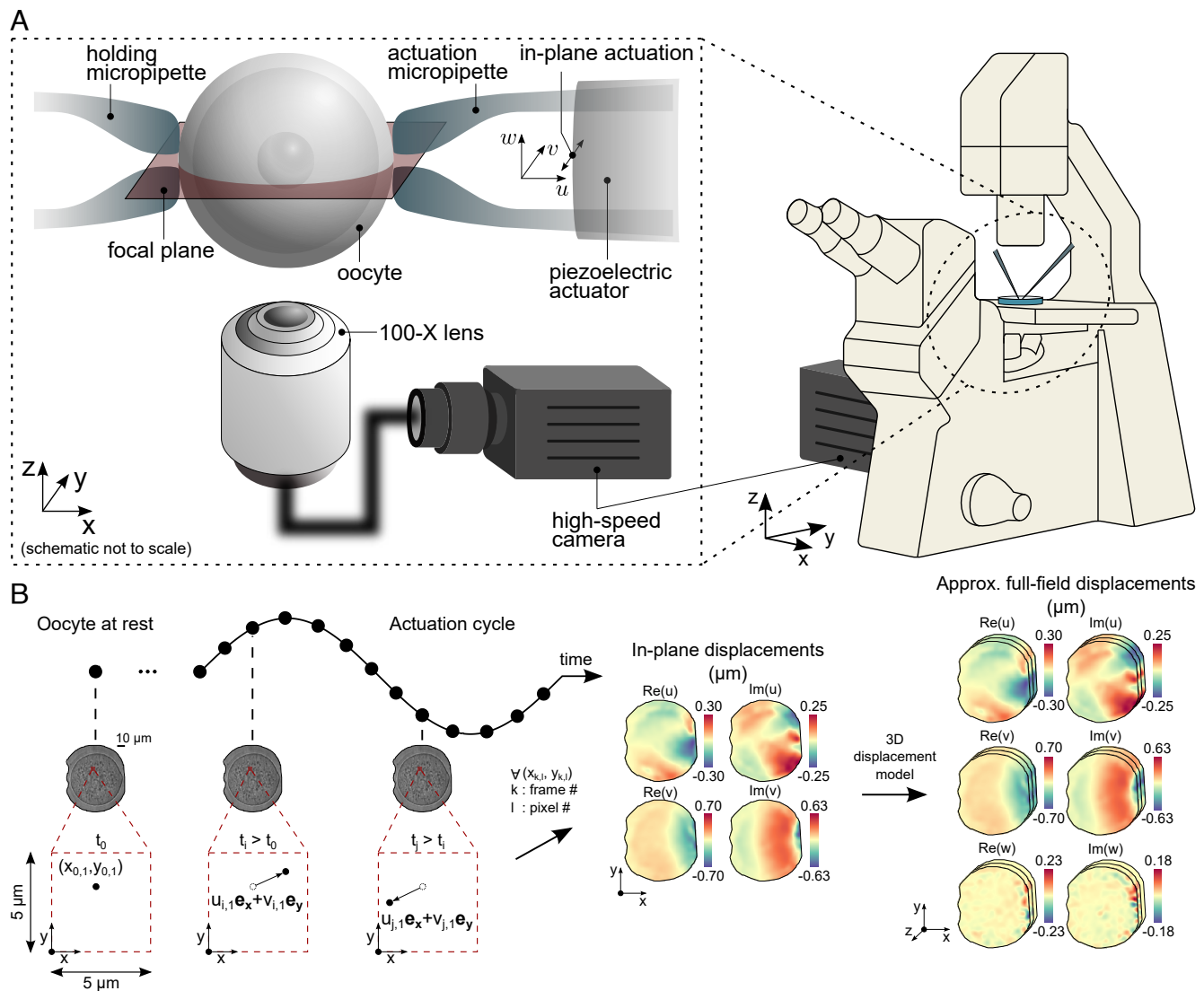
Fig. 1. Optical microelastography in mouse oocytes. (*A*) Experimental setup. The selected oocyte is held by two micropipettes; the *Left* side is immobile, and the *Right* side is connected to a piezoelectric crystal and pulses in the xOy plane. The focal plane is set at the center of the oocyte. A high-speed camera captures images of the oocyte being pulsed by the actuation micropipette. (*B*) Images acquired with the camera at a 200-kHz frame rate during harmonic actuation are processed with an optical-flow method to estimate in-plane displacements (*u* and *v*). A full-field displacement dataset (*u*, *v*, and *w*) is approximated using a 3D oocyte geometry-based model. The procedure is described in *Methods*.

differences with P-values < 0.005 were found between most regions for both moduli.

The variability of the OME and NLI combination was assessed using images acquired through 15 repeated measurement cycles on the same oocyte. Fig. 4 shows reconstructed storage (μ_r) and loss (μ_i) moduli, along with shear stiffness (μ_s) and damping ratio (ξ). The shear stiffness, defined by $\mu_s = 2\frac{|\mu_r + i\mu_i|^2}{\mu_r + |\mu_r + i\mu_i|}$, was computed to allow comparing the presented results with our previous work, which relied on a correlation-based reconstruction technique (passive elastography) (39). A side-by-side examination of previous and actual results is shown in *SI Appendix*, Fig. S1. The damping ratio presented in Fig. 4, defined by $\xi = \frac{\mu_i}{2\mu_r}$, provides information about the relative elastic and viscous contributions of the tissue, where higher values indicate an attenuating fluid-like behavior and lower values indicate an elastic solid-like behavior. The first column shows reconstructed properties from a single measurement, the second column presents distributed values of coregistered property images averaged over the 15

measurements, and the third column depicts corresponding standard deviations expressed in percentage of the pixel-by-pixel property averaged values.

Discussion

A robust method for the viscoelastic characterization of oocytes was presented and applied to freshly collected mouse oocytes. The recovered images presented an unmatched cell structure differentiation based on their distributed viscoelastic properties. Full-field displacement data were approximated through a three-dimensional displacement model, and the storage and loss moduli were reconstructed using a nonlinear inversion algorithm based on reconstruction error minimization. Although the storage modulus, or attenuation-free shear stiffness, is mostly considered in elastography, the viscosity-related behavior of biotissues has also proven to carry important information, notably on oocytes and embryos potential in in vitro fertilization (7), liver
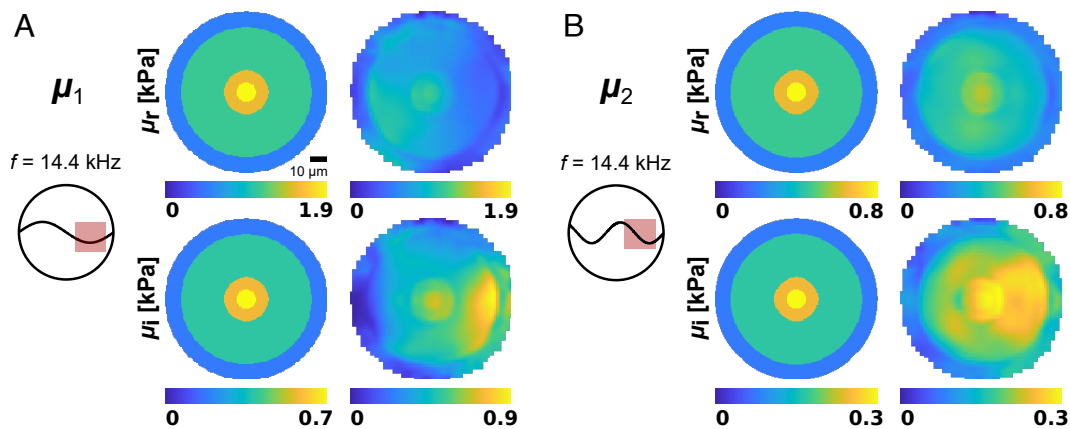
Fig. 2. Viscoelasticity reconstructions performed on simulated displacement data. Panels (*A*) and (*B*) represent the two experiment-based shear modulus distributions used in simulations, $\mu_1 = 2.5 \times \mu_{exp}$ and $\mu_2 = \mu_{exp}$, where μ_{exp} refers to the average distribution observed in experiments (*Methods* section for details). The individual domains in μ_{exp} were set to $\mu_{exp,nucleolus} = 768 + i268$ Pa, $\mu_{exp,nucleus} = 615 + i217$ Pa, $\mu_{exp,cytoplasm} = 444 + i147$ Pa, and $\mu_{exp,zp} = 202 + i68$ Pa. For each simulation, the wavelength and isotropic 30-μm subzone are indicated in the first column of both panels by the sine curve in the spherical oocyte domain and the red square, respectively. For each panel, the second and third columns represent, respectively, the true and reconstructed distributions using the approximated full-field displacements.

tumor types (43), and sex-related differences in brain cortical regions (44).

Kort and Behr (12) recently reviewed and highlighted the needs for better embryo and oocyte selection methods in in vitro fertilization procedures. Specifically, biomechanical properties were estimated critical for the function of these cells. As such, the subcellular viscoelasticity imaging technique presented herein demonstrates relevant criteria and may be used to address cell selection in embryology workflows. Moreover, the following attributes constitute significant advances in the field of microelastography. First, no restrictive assumption on the nature of the elastic field is needed, such as the pure-shear approximation, owing to the boundary value problem involved (Eq. 7), which allows characterizing the material's biomechanics rather than wave properties (speed c or wavelength λ). This is a significant advantage in micron-scale confined cellular domains where the presence of bulk shear waves is not guaranteed, thus challenging the conventional elastic relationship $\mu_s = \rho c^2$, as suggested in ref. 40. Then, the difficult preselection of a rheological model is circumvented by the generalized viscoelasticity equilibrium Eq. 7. Finally, the iterative error minimization approach does not operate on the measured data directly, which ensures a higher tolerance to noise relative to direct inversion techniques and avoids the arbitrary preselection of a motion component owing to the three-dimensional description of the material.

In simulations, the modeled shear modulus distributions were based on the mechanical contrasts recovered from experiments conducted at the same actuation frequency of 14.4 kHz. Fig. 2*A* represents the worst-case scenario where the zone size is smaller than half of the long wavelength induced in the simulated oocyte domain. Individual regions could still be distinguished, but the reconstruction converged to scaled distributions, which is a typical effect in the presence of long wavelengths (45, 46). In Fig. 2*B*, the recovered distributions were closer to the true distributions as the modeled shear modulus values had a lower magnitude and consequently resulted in a wave field with a shorter wavelength. This illustrates that shorter wavelengths relative to the subzone size contribute to more accurate reconstructions. Finally, reconstructions accurate to numerical precision could be achieved in simulations using true instead

of approximated full-field displacement data, as shown in *SI Appendix,* Note 4 and Fig. S4.

In Figs. 3 and 4, an additional structure in the oocyte, the nucleolus, could be identified in comparison with our previous work (39). From Fig. 3 and Table 1, most of the paired oocyte regions showed significant differences in both properties with *P*-values lower than 0.005, even in the case of partially converged reconstructions.

In an average sense, no significant property difference was found between the nucleus on the one hand and the nucleolus and cytoplasm on the other hand across all cells, as shown in Table 1. This may be due to the small thickness of the nucleus, which is encompassed between the nucleolus and the cytoplasm. However, a local property contrast in μ_r and μ_i maps was observed in sufficiently thick portions of the nucleus, as seen in Figs. 3 *E* and *F*, and 4. Similarly, the ZP remains a difficult structure to characterize due to its thinness. In most cases, it is bound by the fluid PS and the external medium (excluded from the geometry), which could alter the displacement estimation and consequently the reconstruction in this region. In both Figs. 3 and 4, the circular fluid PS could be differentiated in recovered images, but the identified property values are considered inaccurate as a viscoelastic model was used in a fluid region. This part of the domain was maintained in the treated geometry in the interest of illustrating the capability of the proposed method to discriminate structural details in live cells.

During the fast imaging process, oocytes receive external vibrations for ≈ 0.75 ms per acquisition cycle, corresponding to a little more than 11.25 ms for the 15 repeated acquisition sessions on the same cell. The multiple measurements allowed by this short time scale increase the reliability of reconstructions through coregistration and pixel-by-pixel averaging. In Fig. 4, the recovered properties, μ_r, μ_i, μ_s, and ξ, were obtained from measurements on the representative oocyte shown in Fig. 3*E*. The averaged reconstructions presented in Fig. 4 show distributions similar to the single measurement case and feature a unique visual contrast where the five oocyte structures can be finely identified in μ_r, μ_i, and μ_s maps. These reconstructions provide superior regional details relative to the damping-free shear stiffness reported in our previous work (39), as shown by the side-by-side
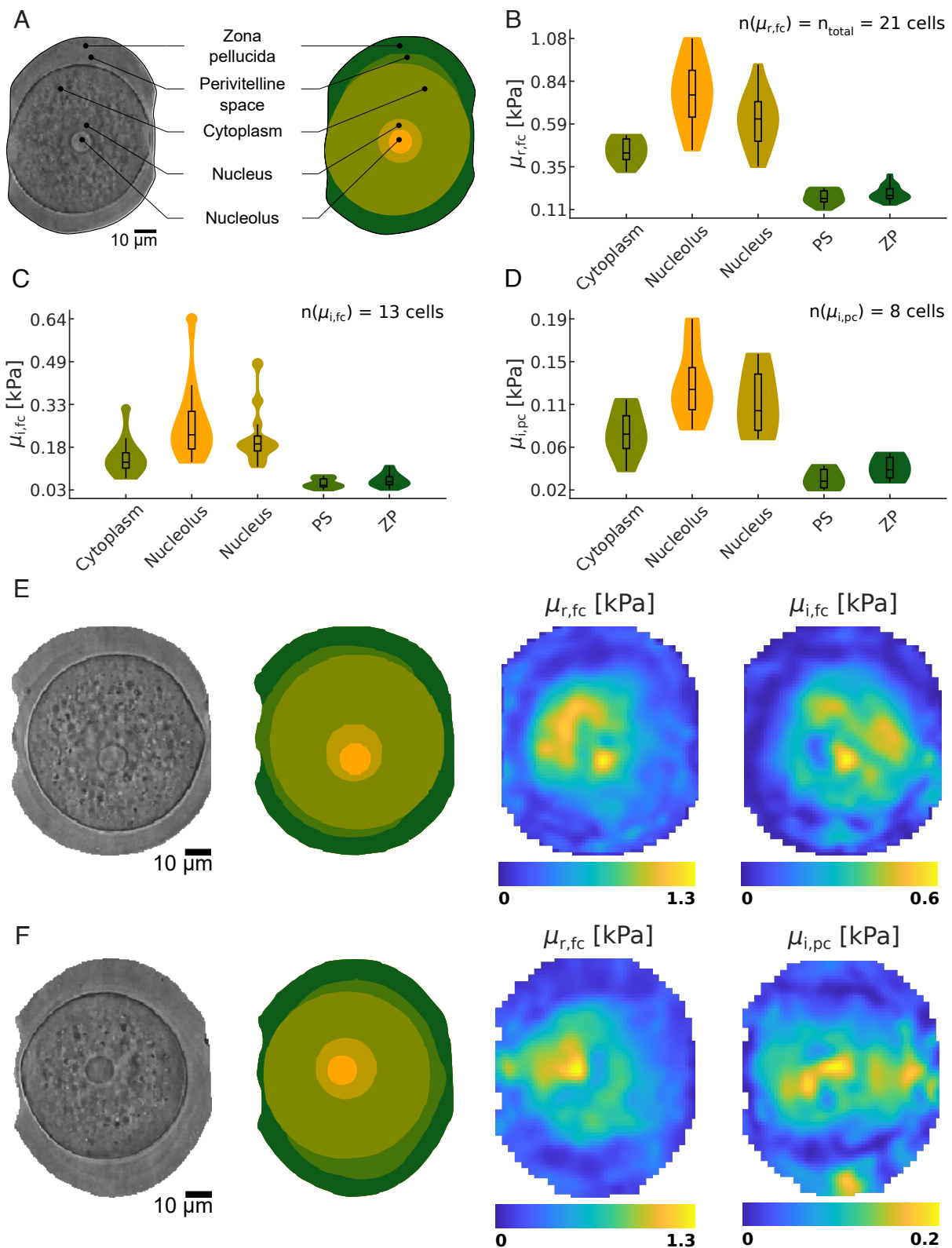
Fig. 3. Storage and loss modulus reconstructions in 21 mouse oocytes. (*A*) Anatomical image of a representative mouse oocyte and corresponding segmented regions. (*B*) Average values of storage modulus reconstructions performed on 21 oocytes. All reconstructions converged to stable distributions ($\mu_{r,fc}$). (*C*) Average values of fully converged loss modulus reconstructions (13 out of 21) in the five segmented regions ($\mu_{r,fc}$). (*D*) Average values of partially converged loss modulus reconstructions (8 out of 21) in the five segmented regions ($\mu_{r,pc}$). (*E*) Representative oocyte for which both the storage and loss modulus reconstructions were complete. Images show the oocyte and corresponding segmented regions and the storage and loss modulus reconstructions ($\mu_{r,fc}$ and $\mu_{i,fc}$, respectively). (*F*) Representative oocyte for which the storage modulus reconstruction was complete and the loss modulus reconstruction was partial. Images show the oocyte and corresponding segmented regions and the storage and loss modulus reconstructions ($\mu_{r,fc}$ and $\mu_{i,pc}$, respectively).

Table 1. Statistical differences between paired regions

P-values	Cyto.–nucleo.	Cyto.–nucl.	Cyto.–PS	Cyto.–ZP	Nucleo.–nucl.	Nucleo.–PS	Nucleo.–ZP	Nucl.–PS	Nucl.–ZP	PS–ZP
$\mu_{r,fc}$	< 0.001	< 0.001	< 0.001	< 0.001	> 0.005	< 0.001	< 0.001	< 0.001	< 0.001	> 0.005
$\mu_{i,fc}$	< 0.005	> 0.005	< 0.001	< 0.001	> 0.005	< 0.001	< 0.001	< 0.001	< 0.001	> 0.005
$\mu_{i,pc}$	< 0.005	> 0.005	< 0.005	< 0.005	> 0.005	< 0.001	< 0.001	< 0.001	< 0.001	> 0.005

Cyto.: cytoplasm, Nucleo.: nucleolus, Nucl.: nucleus, PS: perivitelline space, ZP: zona pellucida.

comparison presented in *SI Appendix*, Fig. S1. Higher variability levels are observed in SD maps of μ_i and ξ reconstructions on edges near the immobilizing pipette where wave illumination is low. Finally, piezo-driven ICSI procedures have been reported to be safe for oocytes and improve survival and fertilization rates in comparison to conventional ICSI (47–49). These particular characteristics demonstrate that the submicron piezo-induced vibrations do not damage the oocyte, even when used to break the plasma membrane. In optical microelastography, the pulsing pipette is noninvasive as it simply laterally sweeps along the surface of the ZP over about 1 μm without breaking it or even touching the plasma membrane, which suggests that optical microelastography should be safe.

Limitations and Future Work

In this work, the measured wave fields have a wavelength on the order of the oocyte diameter. As shown by simulations, this long-wavelength condition challenges absolute mechanical property recovery and likely leads to scaled reconstructions. Although oocyte structures could be differentiated in both simulations and experiments, an absolute property recovery is desirable in view of clinical application. Generating elastic fields of shorter wavelengths requires increasing the actuation frequency. To date, displacement fields suitable for microelastography have been observed at frequencies up to 20 kHz in tissue-mimicking phantoms (40). Further analysis of the frequency content of the displacement data obtained in oocytes specifically, and future work involving mechanical actuators adapted to higher frequency delivery, will help address the usable frequency range in oocyte microelastography.

Oocytes were modeled as heterogeneous, viscoelastic, nearly incompressible, and isotropic biomaterials. Although this characterization reduces model-data mismatch errors related to previous purely elastic and locally homogeneous descriptions (39), additional violation of the current assumptions would contribute to other model-to-data mismatches and result in reconstruction inaccuracies. For instance, oocytes are made of structures with inherent directionality, such as microtubules and microfilaments, and contain porous complexes, notably in the ZP (50, 51). This suggests that anisotropy and poro-elasticity imaging are worth consideration. The effects of a viscoelastic isotropic characterization on a viscoelastic anisotropic or poro-elastic isotropic tissue have been evidenced using magnetic resonance elastography (52–54). Guidelines on the suitability of these material models, established in other tissues (55–59) and at different harmonic actuation regimes (46, 54), will certainly help improve oocyte characterization in future works. The near-incompressible description of oocytes may also be revisited by using a compressible material model (60) and a true full-field displacement dataset. However, the high water content in cells suggests a low level of bulk modulus-based cellular structure differentiability, and an actual incompressible rather than compressible behavior is expected, as described in ref. 61. Ultimately, extension of the single-plane imaging sequence to multiplane and incorporation of 3D motion tracking throughout the acquired slices (62) would further improve the accuracy of the property maps reported in Figs. 3 and 4. It would also eliminate the need for geometry-based displacement modeling and central positioning of the focal plane and thus contribute to a broad application of the proposed method to cells of arbitrary shapes. For instance, the geometry assumptions made in this work no longer hold with metaphase-II stage oocytes and early
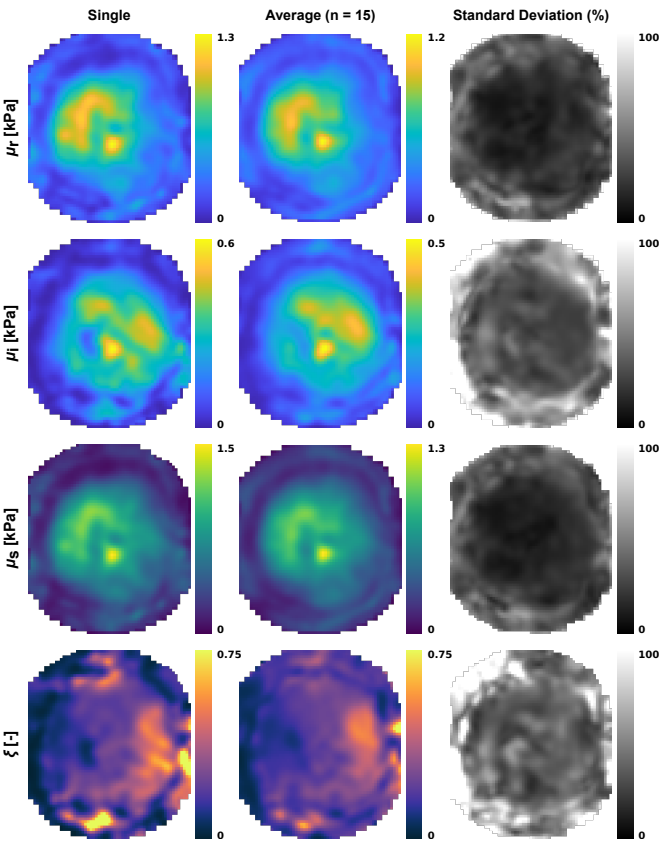

Fig. 4. Viscoelasticity reconstructions in 15 repeated measurements on the same oocyte. Four properties are represented: storage modulus μ_r, loss modulus μ_i, shear stiffness $\mu_S = 2\frac{|\mu_r + i\mu_i|^2}{|\mu_r| + |\mu_r + i\mu_i|}$, and damping ratio $\xi = \frac{\mu_i}{2\mu_r}$. The shear stiffness was computed to allow comparing the presented results with previous work (39). A side-by-side examination of previous and actual results is shown in *SI Appendix*, Fig. S1. The damping ratio is a measure of the relative elastic and viscous contributions of the tissue where higher values indicate an attenuating fluid-like behavior, and lower values indicate a rather elastic solid-like behavior. The first column shows reconstructions performed from a single acquisition cycle. The second column shows distributed values of coregistered reconstructed properties averaged across 15 measurements. The third column shows corresponding pixel-by-pixel standard deviations expressed as a percentage of the mean values.

fertilized embryos, which are clinically more useful than GV-stage oocytes. The acquisition of full-field displacement data would be necessary in this case to validate the overall procedure and avoid potential hurdles to clinical application. Future acquisition of a piezo-driven lens position controller should allow addressing multiplane imaging with adjustable phase offsets by exploiting the harmonic actuation regime.

Work is underway to incorporate a pixel-wise displacement estimation in the pipeline, as opposed to the current region-based method, which will help provide more accurate motion estimates in thin or confined areas such as the nucleus or the zona pellucida, and consequently improve the reconstruction sensitivity in these regions (63). Property maps may also be enhanced in future works by enabling total variation minimization or soft prior regularization (64). Finally, incorporation of the presented microelastography procedure into embryology workflows (11) would help address the detectability limit of subtle cell defects through the processing of larger sample sizes, oocytes at different stages of development, and early fertilized embryos.

Conclusions

Viscoelasticity images of live mouse oocytes were produced noninvasively through the recovery of storage and loss modulus distributions. These previously unseen reconstructions demonstrated unique structural detail levels at a subcellular scale. Based on Yanez et al. (7), there are fair reasons to suspect that oocyte and embryo quality might be reflected in these measurements in a way that might allow predictive selection as an alternative to morphological examination or expensive and invasive preimplantation genetic screenings.

Materials and Methods

Oocyte Imaging. The procedure reported here was conducted in accordance with guidelines of the Institutional Animal Care Committee of the University of Montreal Hospital Research Center, and the study conformed with guidelines of the Canadian Council on Animal Care and the Guide for the Care and Use of Laboratory Animals. Oocyte growth was stimulated by injecting 5 IU of pregnant mare serum gonadotropin (PMSG) to the mouse between 44 and 48 h before collecting oocytes. Ovaries were then extracted and placed in 1 to 2 ml of M2 medium supplemented with 200 nM of 3-isobutyl-1-methyl-xanthine (IBMX), and GV-stage oocytes were recovered by puncturing follicles with a 27-gauge needle. Granulosa cells were removed by successive pipetting and washings in M2+IBMX droplets. Oocytes were then transferred to another M2+IBMX droplet in a dedicated petri dish, itself placed on the platform of an inverted microscope (Leica DM IL LED with $100\times$ lens). Microelastography measurements were made from a total of 21 oocytes, and each oocyte was manipulated using glass micropipettes. The pipette on the left-hand side (ICSI holding pipette) was held fixed while that on the right-hand side was mounted on a piezo-electric pulsing unit (PMM-150FU, Prime Tech Ltd., Tsuchiura, Japan) used for harmonic motion generation in the oocyte. While operating, the pulsing pipette was oscillating laterally in the focal plane of the lens set at the center of the oocyte. The coupling of the piezo-driven ICSI equipment with the micropipette allowed a pulsation between $\approx$ 14 kHz and 16 kHz. A 14.4-kHz actuation provided efficient motion transmission to the oocytes in this specific configuration. Images of the oocyte during the dynamic procedure were acquired at a 200-kHz frame rate with an isotropic pixel resolution of 0.5 μm using a high-speed camera (Photron, FastCam SA-Z, San Diego, USA) for subsequent estimation of local small tissue displacements in the cell (Fig. 1B).

In-Plane Displacement Estimation. Time-harmonic displacements were estimated by applying the Lagrangian speckle model estimator (LSME) algorithm to the image stack of the oocyte under actuation. LSME is based on a Lucas–Kanade optical flow variation where image correlation between two or more frames is performed (65). Here, all displacements were calculated with respect to a reference frame of the oocyte at rest, imaged prior to actuation, to mimic motion encoding in MR elastography and ensure compatibility of the motion data format with the NLI procedure. The choice of LSME's intrinsic parameters (size of interrogating windows and overlapping percentage) was determined by testing different parameter sets on simulated optical images of the oocyte being deformed in time by a harmonic actuation of 14.4 kHz (see the Simulation paragraph below).

3D-Oocyte Displacement Model. Estimated in-plane displacements were processed by a 3D-oocyte displacement model to approximate a full-field displacement dataset (u, v, and w). First, the out-of-plane component w_1 in the measured slice, indicated by the subscript "1", was negated owing to the following assumption and experimental settings:

1) oocytes were assumed spherical, which is in line with common descriptions of GV-stage oocytes (23);
2) the focal plane of the lens was set to cut through the center of the oocyte, along the symmetry plane of the assumed spherical geometry (66); and
3) the pulsing micropipette used to generate motion in the oocyte oscillated along an axis parallel to the focal plane, permitting Dirichlet boundary condition (BC) $w_{1,BC} = 0$ on the boundary of this symmetry plane.

The combination of these three assumptions leads to the hypothesis that $w_1 = 0$. Second, two artificial slices labeled "2" and "3" were derived from BCs and spherical geometry properties as follows. The out-of-plane components w_2 and w_3 in the extra two slices were estimated by assuming an incompressible medium, which is a common characteristic of biological tissues (61). Mathematically, local incompressibility was enforced by:

$$\nabla \cdot \mathbf{u} = \frac{\partial u}{\partial x} + \frac{\partial v}{\partial y} + \frac{\partial w}{\partial z} = 0,$$ [1]

$$\Leftrightarrow w_{i+1} = -\left(\frac{\partial u}{\partial x} + \frac{\partial v}{\partial y}\right)\delta z + w_i,$$ [2]

where δz is the prescribed interslice distance of 1.25 μm. The selection of δz and its impact on the reconstruction are described in *SI Appendix*, Note 5 and illustrated in *SI Appendix*, Figs. S5 and S6. First-order derivatives were approximated using third-order 2D-polynomial projection in 7-7 pixel^2 kernels. Finally, the local symmetry properties of $\frac{\partial u}{\partial z}\big|_1$ and $\frac{\partial v}{\partial z}\big|_1$ in the focal plane (slice 1) were invoked to approximate in-plane displacements in immediate neighbor slices 2 and 3 (*i.e.*, u_2, v_2, u_3, and v_3):

$$\frac{\partial u}{\partial z}\bigg|_1 = \frac{\partial v}{\partial z}\bigg|_1 = 0,$$ [3]

$$\frac{\partial u}{\partial z}\bigg|_2 \approx \frac{\partial v}{\partial z}\bigg|_2 \approx \frac{\partial u}{\partial z}\bigg|_3 \approx \frac{\partial v}{\partial z}\bigg|_3 \approx 0,$$ [4]

which led to:

$$u_1 \approx u_2 \approx u_3,$$ [5]

$$v_1 \approx v_2 \approx v_3.$$ [6]

Simulations. Synthetic 3D displacements were generated in a finite element model of a mouse oocyte assuming a viscoelastic, heterogeneous, nearly incompressible, and isotropic solid as described by Eq. **7**. Simulations were programmed in Comsol Multiphysics using the Matlab interface (Comsol 5.5 and LiveLink for Matlab (Comsol Inc. Stockholm, Sweden); Matlab R2019b, The MathWorks, Massachusetts, USA). The oocyte model consisted of a four-domain geometry made of four concentric spheres representing the nucleolus, the nucleus, the cytoplasm, and the zona pellucida (ZP), as shown in Fig. 1A. The nucleolus had a radius $r_{nucleo} = 5.6$ μm, the nucleus $r_{nucleus} = 12.3$ μm, the cytoplasm $r_{cyto} = 36.7$ μm, and the surrounding sphere binding the ZP $r_{zp} = 45.4$ μm (corresponding to a ZP with thickness of 8.6 μm). Dimensions were extracted from anatomical images of oocytes. Dirichlet boundary conditions were defined on the ZP in circular cross-sections of radii $r_{pip} = 18.0$ μm at opposite locations along the x axis to represent the fixed and pulsing pipettes, as shown in Fig. 1A. Displacements oscillating along the y axis with an amplitude

of 1 µm were prescribed to the pulsed boundary, whereas the held area was maintained fixed (0 µm displacements along each axis). BCs were left unconstrained on the remaining surface of the ZP. Two relative experiment-based shear modulus distributions, μ_1 and μ_2, were considered in the simulations since experimental reconstructions were likely scaled because of the induced long wavelength. The property distribution μ_1 was set by multiplying the shear modulus recovered from experiments, μ_{exp}, by a scaling factor of 2.5 to reproduce the long wavelength condition observed at 14.4 kHz. The second shear modulus distribution μ_2 was set to $\mu_2 = \mu_{exp}$. The μ_{exp} distribution was defined by the average values obtained in each of the segmented regions shown in Fig. 3: $\mu_{exp,nucleolus} = 768 + i268$ Pa, $\mu_{exp,nucleus} = 615 + i217$ Pa, $\mu_{exp,cytoplasm} = 444 + i147$ Pa, and $\mu_{exp,zp} = 202 + i68$ Pa. Density ρ and bulk modulus K were held constant through all simulations at $\rho = 1000$ kg m^{-3} and $K = 2.2 \times 10^9$ Pa.

Once computed, the finite element displacement fields were interpolated on an isotropic grid at the same resolution as the experimental images (0.5 µm). For reconstructions based on true full-field displacement data, the three motion components in a set of contiguous slices were extracted. To mimic the experimental measurements and the full-field approximation procedure, in-plane displacements only were extracted from the central slice of the 3D oocyte model. The complex-valued displacement data were then converted to time displacements by generating a suitable power spectral density and applying the inverse fast Fourier transform using Matlab. The resulting time-domain displacements underwent the preprocessing procedure used for experimental data.

Then, optical images were simulated to select adequate parameters for motion tracking. First, a texture image was generated through a random distribution of gray-scale points convoluted with a $5 \times 5 \times 5$ pixel^3 kernel in a volume surrounding the imaged slice (xOy plane) in the oocyte model. Dynamic deformation images were generated for each time step by forcing each point of the texture image to move a distance given by the computed displacements u_c, v_c, and w_c in the simulation (μ_1 distribution). Finally, LSME was applied to the simulated optical images using successive sets of interrogation window sizes and overlaps. An isotropic size of 10×10 pixel^2 with 90% overlap was found to produce reliable displacement maps and was used in the present work.

Inverse Problem. Originally developed for MR-based viscoelastic property identification, NLI is an optimization-based reconstruction method formulated on the minimization of the mismatch between measured displacements and displacements predicted by a heterogeneous finite-element mechanical model (41, 42). The computational cost of the NLI property update for the complete region of interest is mitigated by decomposing the domain into overlapping subdomains, termed subzones. Subzones are randomly distributed across the domain, processed in parallel, and eventually recombined to form a global property image. Here, oocytes were modeled as a heterogeneous, viscoelastic, nearly incompressible, and isotropic material. The corresponding boundary value problem relating the material's mechanical parameters to the measured displacement field is given by:

$$
\begin{cases}
\nabla \cdot (\mu \nabla \mathbf{u}) + \nabla (\mu \nabla \cdot \mathbf{u} - p) = -\rho \omega^2 \mathbf{u} & \text{in } \Omega, \\
K tr (\boldsymbol{\varepsilon}) = -p & \text{in } \Omega, \\
\mathbf{u} = \mathbf{u}_0 & \text{on } \Gamma_u, \\
\mathbf{n} \cdot \boldsymbol{\sigma}_E = \mathbf{f}_0 & \text{on } \Gamma_\sigma,
\end{cases}
\tag{7}
$$

where Ω is the oocyte domain, $\mathbf{u}$ is the displacement vector (m) containing three components (u, v, and w) along the three axes of the Cartesian coordinate system (x, y, and z, respectively), μ is the complex-valued shear modulus (Pa), p is the pressure field (Pa), ρ is the mass density (kg m^{-3}), ω is the actuation angular frequency (rad s^{-1}), K is the bulk modulus (Pa), tr is the trace operator, $\boldsymbol{\varepsilon}$ is the strain tensor, $\mathbf{u}_0$ is the displacement vector on the domain's boundary Γ_u, $\boldsymbol{\sigma}_E$ is the stress tensor, $\mathbf{n}$ is the unit vector normal to the surface boundary Γ_σ,

and $\mathbf{f}_0$ is the traction force vector. In NLI, boundary conditions are extracted from the measured displacements, so only Γ_u is defined. Parameters ρ and K were assumed known and constant throughout, and the properties of interest were the real and imaginary parts of the complex shear modulus $\mu \equiv \mu_r + \mu_i$, termed storage ($\mu_r \equiv G'$) and loss ($\mu_i \equiv G''$) moduli, respectively. The calculation of the solution to the inverse problem is then formulated as the minimization of the following objective function:

$$
\Phi = \frac{1}{2} (\mathbf{u}_c (\theta) - \mathbf{u}_m)^H (\mathbf{u}_c (\theta) - \mathbf{u}_m),
\tag{8}
$$

where $\mathbf{u}_c$ is the displacement field computed through Eq. **7** using finite-elements, $\mathbf{u}_m$ is the measured displacement field, θ is the vector containing the inferred mechanical properties, and H refers to the complex-conjugate transpose. The property distribution θ that minimizes the objective function Φ is then considered the most likely approximation of the true distribution. The solution to Eq. **7** was computed on a 27-node hexahedral finite-element mesh using quadratic shape functions. Displacement and property meshes had the same resolution as the displacement data. Subzones had an isotropic size of 30 µm^3 with a 20% overlap in all reconstructions. The selection of the subzone size for the nonlinear inversion is described in *SI Appendix*, Note 5 and illustrated in *SI Appendix*, Figs. S5 and S6. The high resolution of optical images (0.5 µm, isotropic) allowed down-sampling of the displacement data by a factor of 2.5, permitting relatively large zone sizes while maintaining a reasonable runtime per iteration. The conjugate gradient (CG) method was used to solve the inverse problem. A maximum of 1000 global iterations was allowed in experiments and in the first simulation (μ_1 distribution), and CG involved 1 CG iteration per zone from global iterations 1 to 10, 3 CG iterations from global iterations 11 to 300, and 6 CG iterations from global iterations 301 to 1,000. In the second simulation (μ_2 distribution), 500 global iterations were allowed, and CG involved 1 CG iteration per zone from global iterations 1 to 10, 3 CG iterations from global iterations 11 to 200, and 3 CG iterations from global iterations 201 to 500. Gaussian smoothing with a filter width of 1.2 µm was used to stabilize the reconstruction procedure, as in standard MR elastography–based NLI reconstructions. As in a vast majority of elastography protocols, a homogeneous density of 1,000 kg m^{-3} was assumed, and the bulk modulus was set to a homogeneous value $K = 2.2 \times 10^9$ Pa reflecting tissue incompressibility and low spatial variations, as described in ref. 61. Average reconstruction maps in Fig. 4 were obtained by coregistering anatomical images of the same oocyte at rest for each of the 15 acquisition cycles using an affine geometry transformation (translation, rotation, scale, and shear).

Data, Materials, and Software Availability. Some study data available [Raw data (optical image sequences) are available upon request to the corresponding author. Data are archived at the University of Montreal Hospital Research Center].

Author affiliations: [a]Laboratory of Biorheology and Medical Ultrasonics, University of Montreal Hospital Research Center, Montreal, QC H2X 0A9, Canada; [b]Mechanical Engineering Department, University of Sherbrooke, Sherbrooke, QC J1K 2R1, Canada; [c]Oocyte and Embryo Research Laboratory, University of Montreal Hospital Research Center, Montreal, QC H2X 0A9, Canada; [d]Department of Obstetrics and Gynecology, University of Montreal, Montreal, QC H3T 1J4, Canada; and [e]Department of Radiology, Radio-Oncology and Nuclear Medicine, and Institute of Biomedical Engineering, University of Montreal, Montreal, QC H3T 1J4, Canada

1. S. Hirsch, J. Braun, I. Sack, *Magnetic Resonance Elastography: Physical Background and Medical Applications* (John Wiley and Sons, 2017).
2. I. Z. Nenadic *et al.*, *Section VII: Clinical Elastography Applications* (John Wiley and Sons, 2019), pp. 471–566.
3. H. Li *et al.*, Viscoelasticity imaging of biological tissues and single cells using shear wave propagation. *Front. Phys.* **9**, 66–103 (2021).
4. G. T. Charras, T. J. Mitchison, L. Mahadevan, Animal cell hydraulics. *J. Cell Sci.* **122**, 3233–3241 (2009).

5. S. E. Cross, Y. S. Jin, J. Rao, J. K. Gimzewski, Nanomechanical analysis of cells from cancer patients. *Nat. Nanotechnol.* **2**, 780–783 (2007).
6. N. Bufi *et al.*, Human primary immune cells exhibit distinct mechanical properties that are modified by inflammation. *Biophys. J.* **108**, 2181–2190 (2015).
7. L. Z. Yanez, J. Han, B. B. Behr, R. A. R. Pera, D. B. Camarillo, Human oocyte developmental potential is predicted by mechanical properties within hours after fertilization. *Nat. Commun.* **7**, 10809 (2016).
8. L. Andolfi *et al.*, Investigation of adhesion and mechanical properties of human glioma cells by single cell force spectroscopy and atomic force microscopy. *PLoS ONE* **9**, e112582 (2014).
9. M. Lekka, Discrimination between normal and cancerous cells using AFM. *BioNanoScience* **6**, 65–80 (2016).
10. P. Rosendahl *et al.*, Real-time fluorescence and deformability cytometry. *Nat. Methods* **15**, 355–358 (2018).
11. L. Z. Yanez, D. B. Camarillo, Microfluidic analysis of oocyte and embryo biomechanical properties to improve outcomes in assisted reproductive technologies. *Mol. Hum. Rep.* **23**, 235–247 (2017).
12. J. Kort, B. Behr, Biomechanics and developmental potential of oocytes and embryos. *Fert. Steril.* **108**, 738–741 (2017).
13. J. Guck, R. Chilvers Edwin, Mechanics meets medicine. *Sci. Transl. Med.* **5**, 212fs41 (2013).
14. M. Papi *et al.*, Mechanical properties of zona pellucida hardening. *Eur. Biophys. J.* **39**, 987–992 (2010).
15. Y. Murayama *et al.*, Mouse zona pellucida dynamically changes its elasticity during oocyte maturation, fertilization and early embryo development. *Hum. Cell* **19**, 119–125 (2006).
16. Y. Murayama *et al.*, Elasticity measurement of zona pellucida using a micro tactile sensor to evaluate embryo quality. *J. Mamm. Ova Res.* **25**, 8–16 (2008).
17. A. Chaigne *et al.*, A soft cortex is essential for asymmetric spindle positioning in mouse oocytes. *Nat. Cell Biol.* **15**, 958–966 (2013).
18. A Chaigne *et al.*, A narrow window of cortical tension guides asymmetric spindle positioning in the mouse oocyte. *Nat. Commun.* **6**, 6027 (2015).
19. I. Bennabi *et al.*, Artificially decreasing cortical tension generates aneuploidy in mouse oocytes. *Nat. Commun.* **11**, 1649 (2020).
20. A. I. Mihajlović, J. Haverfield, G. FitzHarris, Distinct classes of lagging chromosome underpin age-related oocyte aneuploidy in mouse. *Dev. Cell* **56**, 2273–2283 (2021).
21. I. Krause *et al.*, Characterization of the injection funnel during intracytoplasmic sperm injection reflects cytoplasmic maturity of the oocyte. *Fertil. Steril.* **106**, 1101–1106 (2016).
22. T. Ebner *et al.*, Developmental competence of oocytes showing increased cytoplasmic viscosity. *Hum. Reprod.* **18**, 1294–1298 (2003).
23. T. Shen *et al.*, Separating the contributions of zona pellucida and cytoplasm in the viscoelastic response of human oocytes. *Acta Biomater.* **85**, 253–262 (2019).
24. Y. Murayama, C. E. Constantinou, S. Omata, Micro-mechanical sensing platform for the characterization of the elastic properties of the ovum via uniaxial measurement. *J. Biomech.* **37**, 67–72 (2004).
25. Y. Murayama, S. Omata, Fabrication of micro tactile sensor for the measurement of micro-scale local elasticity. *Sens. Actuators A: Phys.* **109**, 202–207 (2004).
26. X. Liu, J. Shi, Z. Zong, K. T. Wan, Y. Sun, Elastic and viscoelastic characterization of mouse oocytes using micropipette indentation. *Ann. Biomed. Eng.* **40**, 2122–2130 (2012).
27. S. Yu, K. T. Wan, K. P. Roberts, J. C. Bischof, B. J. Nelson, Mechanical property characterization of mouse zona pellucida. *IEEE Trans. NanoBiosci.* **2**, 279–286 (2003).
28. A. Boccaccio *et al.*, Nanoscale characterization of the biomechanical hardening of bovine zona pellucida. *J. R. Soc. Interface* **9**, 2871–2882 (2012).
29. L. Andolfi *et al.*, Planar AFM macro-probes to study the biomechanical properties of large cells and 3D cell spheroids. *Acta Biomater.* **94**, 505–513 (2019).
30. Y. F. Dufrêne, D. Martínez-Martín, I. Medalsy, D. Alsteens, D. J. Müller, Multiparametric imaging of biological systems by force–distance curve-based AFM. *Nat. Methods* **10**, 847–854 (2013).
31. W. W. Ahmed *et al.*, Active mechanics reveal molecular-scale force kinetics in living oocytes. *Biophys. J.* **114**, 1667–1679 (2018).
32. P. H. Wu *et al.*, A comparison of methods to assess cell mechanical properties. *Nat. Methods* **15**, 491–498 (2018).
33. D. R. Gossett *et al.*, Hydrodynamic stretching of single cells for large population mechanical phenotyping. *Proc. Natl. Acad. Sci. U.S.A.* **109**, 7630–7635 (2012).
34. S. Byun *et al.*, Characterizing deformability and surface friction of cancer cells. *Proc. Natl. Acad. Sci. U.S.A.* **110**, 7580–7585 (2013).
35. J. R. Lange *et al.*, Microconstriction arrays for high-throughput quantitative measurements of cell mechanical properties. *Biophys. J.* **109**, 26–34 (2015).
36. A. Mietke *et al.*, Extracting cell stiffness from real-time deformability cytometry: Theory and experiment. *Biophys. J.* **109**, 2023–2036 (2015).
37. G. Scarcelli *et al.*, Noncontact three-dimensional mapping of intracellular hydromechanical properties by Brillouin microscopy. *Nat. Methods* **12**, 1132–1134 (2015).
38. K. Elsayad *et al.*, Mapping the subcellular mechanical properties of live cells in tissues with fluorescence emission–Brillouin imaging. *Sci. Signaling* **9**, rs5 (2016).
39. P. Grasland-Mongrain *et al.*, Ultrafast imaging of cell elasticity with optical microelastography. *Proc. Natl. Acad. Sci. U.S.A.* **115**, 861–866 (2018).
40. G. Laloy-Borgna, A. Zorgani, S. Catheline, Micro-elastography: Toward ultrasonic shear waves in soft solids. *Appl. Phys. Lett.* **118**, 113701 (2021).
41. E. E. W. Van Houten, K. D. Paulsen, M. I. Miga, F. E. Kennedy, J. B. Weaver, An overlapping subzone technique for MR-based elastic property reconstruction. *Mag. Res. Med.* **42**, 779–786 (1999).
42. M. D. J. McGarry *et al.*, Multiresolution MR elastography using nonlinear inversion. *Med. Phys.* **39**, 6388–6396 (2012).
43. P. Garteiser *et al.*, MR elastography of liver tumours: Value of viscoelastic properties for tumour characterisation. *Eur. Radiol.* **22**, 2169–2177 (2012).
44. L. V. Hiscox *et al.*, Standard-space atlas of the viscoelastic properties of the human brain. *Hum. Brain Map.* **41**, 5282–5300 (2020).
45. S. W. Gordon-Wylie *et al.*, MR elastography at 1 Hz of gelatin phantoms using 3D or 4D acquisition. *J. Magnet. Res.* **296**, 112–120 (2018).
46. M. McGarry *et al.*, Uniqueness of poroelastic and viscoelastic nonlinear inversion MR elastography at low frequencies. *Phys. Med. Biol.* **64**, 075006 (2019).
47. Y. Fujii, Y. Endo, S. Mitsuhata, M. Hayashi, H. Motoyama, Evaluation of the effect of piezo-intracytoplasmic sperm injection on the laboratory, clinical, and neonatal outcomes. *Reprod. Med. Biol.* **19**, 198–205 (2020).
48. K. Furuhashi *et al.*, Piezo-assisted ICSI improves fertilization and blastocyst development rates compared with conventional ICSI in women aged more than 35 years. *Reprod. Med. Biol.* **18**, 357–361 (2019).
49. K. Hiraoka, S. Kitamura, M. Kuwayama, Piezo-ICSI using ultra-thin needle dramatically improves oocyte survival and fertilization without detrimental effect on embryo development and implantation ability as compared with conventional-ICSI. *Fertil. Steril.* **102**, e32 (2014).
50. A. R. Grover, F. E. Fegley, T. V. Duncan, F. E. Duncan, *The Oocyte*, M. K. Skinner, Ed. (Academic Press, Oxford, 2018), pp. 21–28.
51. A. Stracuzzi, J. Dittmann, M. Bol, A. E. Ehret, Visco- and poroelastic contributions of the zona pellucida to the mechanical response of oocytes. *Biomech. Mod. Mechanobiol.* **20**, 751–765 (2021).
52. A. T. Anderson *et al.*, Observation of direction-dependent mechanical properties in the human brain with multi-excitation MR elastography. *J. Mech. Behav. Biomed. Mater.* **59**, 538–546 (2016).
53. M. McGarry *et al.*, A heterogenous, time harmonic, nearly incompressible transverse isotropic finite element brain simulation platform for MR elastography. *Phys. Med. Biol.* **66**, 055029 (2021).
54. M. D. J. McGarry *et al.*, Suitability of poroelastic and viscoelastic mechanical models for high and low frequency MR elastography. *Med. Phys.* **42**, 947–957 (2015).
55. B. Babaei *et al.*, Magnetic resonance elastography reconstruction for anisotropic tissues. *Med. Image Anal.* **74**, 102212 (2021).
56. M. McGarry *et al.*, Mapping heterogenous anisotropic tissue mechanical properties with transverse isotropic nonlinear inversion MR elastography. *Med. Image Anal.* **78**, 102432 (2022).
57. D. Jyoti *et al.*, Quantifying stability of parameter estimates for in vivo nearly incompressible transversely-isotropic brain MR elastography. *Biomed. Phys. Eng. Exp.* **8**, 035015 (2022).
58. D. R. Smith *et al.*, Anisotropic mechanical properties in the healthy human brain estimated with multi-excitation transversely isotropic MR elastography. *Brain Multiphys.* **3**, 100051 (2022).
59. D. Jyoti *et al.*, Transversely-isotropic brain in vivo MR elastography with anisotropic damping. *J. Mech. Behav. Biomed. Mater.* **141**, 105744 (2023).
60. E. E. W. Van Houten, M. M. Doyley, F. E. Kennedy, K. D. Paulsen, J. B. Weaver, A three-parameter mechanical property reconstruction method for MR-based elastic property imaging. *IEEE Trans. Med. Imaging* **24**, 311–324 (2005).
61. A. P. Sarvazyan, O. V. Rudenko, S. D. Swanson, J. B. Fowlkes, S. Y. Emelianov, Shear wave elasticity imaging: A new ultrasonic technology of medical diagnostics. *Ultrasound Med. Biol.* **24**, 1419–1435 (1998).
62. M. Alessandrini *et al.*, Detailed evaluation of five 3D speckle tracking algorithms using synthetic echocardiographic recordings. *IEEE Trans. Med. Imaging* **35**, 1915–1926 (2016).
63. H. Li, J. Poree, B. Chayer, M. H. Roy Cardinal, G. Cloutier, Parameterized strain estimation for vascular ultrasound elastography with sparse representation. *IEEE Trans. Med. Imaging* **39**, 3788–3800 (2020).
64. M. McGarry *et al.*, Including spatial information in nonlinear inversion MR elastography using soft prior regularization. *IEEE Trans. Med. Imaging* **32**, 1901–1909 (2013).
65. J. Poree, D. Garcia, B. Chayer, J. Ohayon, G. Cloutier, Noninvasive vascular elastography with plane strain incompressibility assumption using ultrafast coherent compound plane wave imaging. *IEEE Trans. Med. Imaging* **34**, 2618–2631 (2015).
66. K. Aki, P. G. Richards, *Elastic Waves from a Point Dislocation Source* (University Science Books, 2002), pp. 63–117.